Phonon transport in freestanding SrTiO$_3$ down to the monolayer limit

Qi Wang [ORCID],[1,*] Chen Wang,[2,*] Cheng Chi,[3] Niuchang Ouyang [ORCID],[2] Ruiqiang Guo [ORCID],[1,†] Nuo Yang,[4,‡] and Yue Chen [ORCID][2,§]

[1]*Thermal Science Research Center, Shandong Institute of Advanced Technology, Jinan, Shandong Province 250103, China*
[2]*Department of Mechanical Engineering, The University of Hong Kong, Pokfulam Road, Hong Kong SAR, China*
[3]*Key Laboratory of Power Station Energy Transfer Conversion and System of Ministry of Education, School of Energy Power and Mechanical Engineering, North China Electric Power University, Beijing 102206, China*
[4]*State Key Laboratory of Coal Combustion, School of Energy and Power Engineering, Huazhong University of Science and Technology, Wuhan 430074, China*

Perovskites down to the monolayer limit have emerged and have attracted increased interest due to their two-dimensional nature with potentially novel physical properties. Here, we investigate the phonon transport in the oxide perovskite SrTiO$_3$ with thicknesses from the monolayer limit to 10 nm by constructing an accurate first-principles machine-learning potential and combining it with the Boltzmann transport equation and homogeneous nonequilibrium molecular dynamics simulations. Compared to its bulk counterpart, the phonon dispersion relation of monolayer SrTiO$_3$ is insensitive to temperature, and the calculated in-plane thermal conductivity of monolayer SrTiO$_3$ is much larger than that of bulk SrTiO$_3$, which mainly results from the unique out-of-plane atomic vibrations in monolayer SrTiO$_3$. The thermal conductivity of SrTiO$_3$ thin film first decreases and then approaches the bulk value as thickness increases from the monolayer limit to 10 nm. The hardening of the out-of-plane acoustic phonon branch and the transition of low-frequency optical phonons can explain the observed trend in thermal conductivity transitions. Our study demonstrates that monolayer SrTiO$_3$ has a higher thermal conductivity than its bulk counterpart with covalent bonds at the first-principles level of accuracy, and dimension reduction has a weak inhibition on phonon transport in freestanding atomically smooth SrTiO$_3$ thin films, which furthers the understanding of phonon transport in two-dimensional perovskite thin films.

I. INTRODUCTION

Perovskites have demonstrated remarkable potential in various applications such as photovoltaic [1,2], ferroelectric [3], and energy conversion/storage applications [4,5]. Recently, two-dimensional (2D) perovskites have emerged for their tunable structures [6] and physical properties such as carrier mobility [7], band gap [8,9], and dielectric constant [10]. For example, freestanding oxide perovskite SrTiO$_3$ thin films with different thicknesses, especially the one down to the monolayer limit, have been synthesized [11]. Unlike traditional 2D materials, e.g., graphene and silicene, whose bulk and multilayer counterparts are stacked by van der Waals interactions, the bulk and thin-film counterparts of monolayer SrTiO$_3$ share covalent bonds across the thickness direction, which may lead to the discovery of novel physical properties in 2D SrTiO$_3$ thin films. Recent studies have demonstrated that ultrahigh-dielectric-constant single-crystalline SrTiO$_3$ ultrathin films, with their elastic and 2D nature, can be used to fabricate short-channel transistors with promising performance [10].

When utilizing the emerging 2D perovskites including 2D SrTiO$_3$ thin films in various electronic devices, their thermal properties are the key factor in architecture design for thermal management. However, due to phase transitions and the strong anharmonicity of SrTiO$_3$ and other perovskites, accurately describing phonon transport in perovskites is nontrivial [12,13]. Recently, the phonon properties of bulk SrTiO$_3$ have been investigated with first-principles-based calculations. Using density functional theory (DFT) or a DFT-based machine-learning potential method, the anharmonic phonon properties and thermal conductivity of bulk SrTiO$_3$ have been examined [13–15] through the temperature-dependent effective potential (TDEP) method [16,17] or the self-consistent phonon (SCPH) theory [18], and the calculated thermal conductivity is in good agreement with experimental measurements [13,15]. Anharmonic phonon renormalization, temperature-dependent interatomic force constants (IFCs), and four-phonon scattering are regarded as important factors in accurately describing the phonon transport properties in bulk SrTiO$_3$. The phonon thermal Hall effect [19], electron-phonon interactions [20], and phonon hydrodynamics [21] of bulk SrTiO$_3$ were also extensively investigated. However, the in-plane phonon transport properties and thermal conductivity of 2D SrTiO$_3$ thin films with different thicknesses remain unexplored. The effects of phonon renormalization and high-order phonon scattering on phonon transport are obscure for 2D SrTiO$_3$ thin films. As the thickness of the perovskite thin films used in electronic devices is now down to sub-10 nm, heat dissipation becomes an inevitable issue, and a deeper understanding of the size-thermal-conductivity relationship is necessary.

*These authors contributed equally to this work.
†ruiqiang.guo@iat.cn
‡nuo@hust.edu.cn
§yuechen@hku.hk

Capturing the thickness-dependent thermal properties of semiconductors in the nanoscale regime is always fundamental yet essential for their applications in electronic devices. For example, the in-plane thermal conductivity of Si thin films with different thicknesses was thoroughly studied via theoretical calculations [22–24] and experimental measurements [25,26]. Compared to the bulk, largely suppressed in-plane phonon transport in ultrathin Si films is revealed. Thickness-dependent in-plane thermal transport in many 2D materials and their multilayer van der Waals materials [27,28] were also investigated to achieve tunable thermal properties. As for 2D $SrTiO_3$ thin films with increased thickness, the calculation of in-plane thermal conductivity through direct implementation of first-principles methods presents a formidable challenge. Machine-learning potentials (MLPs) that merge the accuracy of first-principles calculations with the efficiency of empirical potentials are favorable candidates for enabling accurate atomic simulations of the phonon transport of complex systems [29–32]. MLPs have achieved great success in studying phonon transport in various systems [33,34]. However, using molecular dynamics (MD) simulations to extract the thermal conductivity of $SrTiO_3$ thin films with up to 10 nm thickness requires a long simulation time, which is still a challenge even for MLPs. Fan *et al.* developed an MLP called a neuroevolution potential (NEP) [35,36] and implemented it in the graphics processing units (GPU) to speed up MD simulations, which can achieve first-principles accuracy and significantly improve computational efficiency. Here, by constructing an accurate NEP for $SrTiO_3$ thin films and using the Boltzmann transport equation (BTE) and /or homogeneous nonequilibrium molecular dynamics (HNEMD) simulations [37], we demonstrate that the phonon dispersion of monolayer $SrTiO_3$ is insensitive to temperature and the in-plane thermal conductivity is much larger than that of bulk $SrTiO_3$. Our detailed analysis reveals that the pure out-of-plane atomic vibrations in monolayer $SrTiO_3$ and the consequent quadratic phonon dispersion relation near the Γ point induce an enhanced contribution of low-frequency phonons to thermal conductivity. We also extract the thickness-dependent in-plane thermal conductivity of $SrTiO_3$ thin films with thickness up to 10 nm and identify that the change of the out-of-plane acoustic (ZA) and low-frequency optical phonon branches with thickness causes the observed trend in thermal conductivity transitions.

II. METHOD

We develop an accurate NEP for freestanding $SrTiO_3$ thin films using multiple representative configurations based on first-principles calculations. The projector augmented-wave (PAW) method [38] and Perdew-Burke-Ernzerhof revised for solids (PBEsol) exchange-correlation functional [39] were chosen for DFT optimizations and calculations. The energy cutoff was set to 550 eV, and the energy and atomic force convergence criteria were set to 10^{-8} eV and 10^{-6} eV/Å, respectively. The training data set was prepared following an active learning strategy [29,40]. First, *ab initio* MD (AIMD) simulations [41] with a time step of 2 fs and 500 steps were performed for supercells of cubic $SrTiO_3$ and freestanding thin films with thicknesses of 5.97, 10.02, and 13.94 Å at 300,

TABLE I. Hyperparameters for the NEP model.

Parameter	Value	Parameter	Value
r_c^R	8	r_c^A	5
n_{max}^R	12	n_{max}^A	8
N_{bas}^R	12	n_{bas}^A	8
l_{max}^{3b}	4	l_{max}^{4b}	2
N_{neu}	50	λ_1	0.05
λ_2	0.05	λ_e	1
λ_f	1	λ_v	0.1
N_{bat}	428	N_{pop}	50
N_{gen}	4×10^5		

500, and 700 K. Only the Γ point was used for the k-point integration in AIMD simulations. The initial training set was selected to include configurations every 10 steps. Then, classical MD simulations using the LAMMPS package [42] with the pretrained potential and a total of 1 ns for the active learning process were conducted for all systems and temperatures. Finally, 1705 configurations were selected for accurate DFT calculations with a $3 \times 3 \times 3$ ($3 \times 3 \times 1$) k-point mesh for the bulk (thin film) $SrTiO_3$ to obtain the energies, atomic forces, and virials. In addition, 189 configurations including 50 configurations of the 2.2-nm-thick thin film not in the training set were selected from $SrTiO_3$ MD trajectories to form the cross-validation set.

The final 1705 configurations with their energies, atomic forces, and virials were used to train an accurate NEP. The hyperparameter values used in the GPUMD package for the training are listed in Table I. Compared to the DFT calculations, the obtained NEP for $SrTiO_3$ predicts consistent energies, atomic forces, and virials for the training and cross-validation configurations, as shown in Figs. S1 and S2 [43]. For the training set, the root mean square errors (RMSEs) of energies, forces, and virials are 0.60 meV/atom, 59.0 meV/Å, and 7.89 meV/atom, respectively. For the validation set, the RMSEs of energies, forces, and virials are 0.81 meV/atom, 68.7 meV/Å, and 6.87 meV/atom, respectively. To further confirm the ability of the constructed NEP model in predicting phonon properties, harmonic phonon dispersion relations of $SrTiO_3$ with thicknesses of 5.97, 10.02, and 13.94 Å were calculated using the finite displacement method with DFT and NEP model and compared in Fig. S3 [43]. The lattice thermal conductivities of the monolayer and 1.0-nm-thick $SrTiO_3$ thin film calculated from the DFT and NEP are listed in Table S1 [43]. Good agreements are achieved between the NEP and DFT results, demonstrating the capacity of the NEP for phonon calculations of $SrTiO_3$ thin films.

With the NEP, the renormalized phonon dispersions of the monolayer and $SrTiO_3$ thin films were calculated using the TDEP method. The nonanalytic correction to the dynamic matrix was considered within the phonopy package [44]. We adopted both the BTE method as implemented in the ShengBTE [45] and FourPhonon [46] packages and the HNEMD simulations as implemented in the GPUMD package to calculate the lattice thermal conductivity of monolayer $SrTiO_3$. In the BTE method, phonon anharmonicity up to
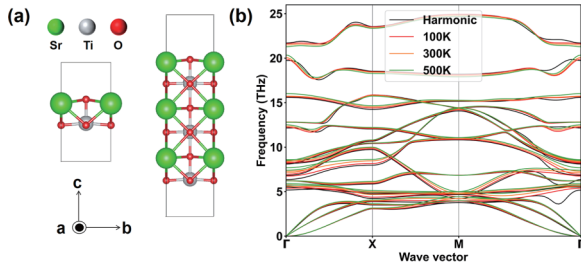
FIG. 1. (a) Crystal structures of $SrTiO_3$ monolayer (left) and thin film with a thickness of 1.4 nm (right). (b) Harmonic and renormalized phonon dispersions at different temperatures.

FIG. 2. Phonon DOS of monolayer, bulk, and $SrTiO_3$ thin film with 1.0 nm thickness at 300 K.

four-phonon scattering was included, and in the HNEMD method, a small driving force applied to each atom was carefully tested (see the Supplemental Material [43]) and chosen as 1.0×10^{-4} Å^{-1}. HNEMD simulations were also used to calculate lattice thermal conductivities of $SrTiO_3$ thin films with different thicknesses. The thickness of a thin film is defined as the summation of the largest vertical distance between two surface atoms and their van der Waals radii, which is consistent with the thickness definition for other 2D materials [47]. The largest thickness in our simulations is 10 nm. More calculation details are included in the Supplemental Material [43].

III. PHONON TRANSPORT IN MONOLAYER STRONTIUM TITANATE

Bulk $SrTiO_3$ exhibits a cubic crystal structure above 105 K, and the harmonic phonon dispersion of the cubic phase shows an imaginary frequency [13,18]. Its renormalized phonon dispersion shows an obvious temperature dependence as revealed in our previous work [13]. For monolayer $SrTiO_3$ [the crystal structure is shown in Fig. 1(a)], its harmonic phonon dispersion calculated with the finite displacement method and the renormalized phonon dispersions at different temperatures calculated with the TDEP method are displayed in Fig. 1(b). The renormalized phonon dispersion of the monolayer at different temperatures resembles the harmonic one and demonstrates a weak temperature dependence. It is noticed that the octahedron consisting of one Ti atom and its six adjacent O atoms in bulk $SrTiO_3$ is broken in monolayer $SrTiO_3$, possibly leading to modified atomic vibrational modes and affecting the lattice anharmonicity of monolayer $SrTiO_3$. We also display the temperature-dependent third and fourth IFC values in Fig. S5 [43], and only a small difference is observed among IFCs at different temperatures. The weak temperature dependence of renormalized phonon dispersions and high-order IFCs of monolayer $SrTiO_3$ is distinct from its bulk counterpart. In bulk $SrTiO_3$, lattice anharmonicity is related to the tilting and rotation of octahedrons, while in monolayer $SrTiO_3$, the octahedral atomic vibrations are missing. In addition, the ZA phonon branch of monolayer $SrTiO_3$ near the Γ point shows a strictly quadratic dispersion similar to those of other 2D materials [48,49], while the transverse acoustic (TA) phonon branch of bulk $SrTiO_3$ is linear. The phonon density of states (DOS) of monolayer $SrTiO_3$ at low frequency also shows a much larger portion than bulk
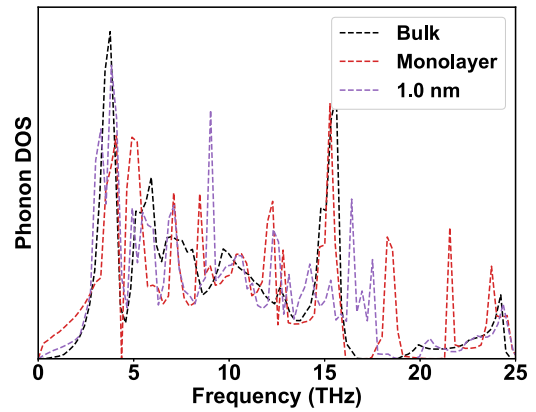
$SrTiO_3$ (see Fig. 2), demonstrating the influence of quadratic dispersion of the ZA phonon branch on phonon properties. In contrast, the DOS of a 1.0-nm-thick $SrTiO_3$ thin film at low frequency shows a small difference compared to the bulk value.

With the NEP, we first determined the thermal conductivity of bulk $SrTiO_3$ at 300 K under the BTE scheme to be 9.2 W/mK, close to the HNEMD value of 8.5 W/mK, and both results are also in good agreement with previous calculations [13–15] and measurements [15,50]. Using the temperature-dependent second, third, and fourth IFCs and the BTE method, we calculated the in-plane thermal conductivity of monolayer $SrTiO_3$ from 100 to 700 K, as plotted in Fig. 3. The HNEMD results are also displayed for comparison. Four-phonon scattering shows a weak influence on the thermal conductivity of monolayer $SrTiO_3$ at 300 K (only 5.5% reduction) compared to the bulk [13]. The thermal conductivities from both methods at different temperatures show good consistency. The thermal conductivity of monolayer $SrTiO_3$ is higher than that of bulk $SrTiO_3$ at 300 K (BTE: 13.9 vs 9.2; HNEMD: 10.5 vs 8.5; unit: W/mK), different from the expectation that classical size effect suppresses phonon transport in covalent solids [22,51]. In Fig. 4, we plot the cumulative thermal conductivity of both bulk and monolayer $SrTiO_3$. For
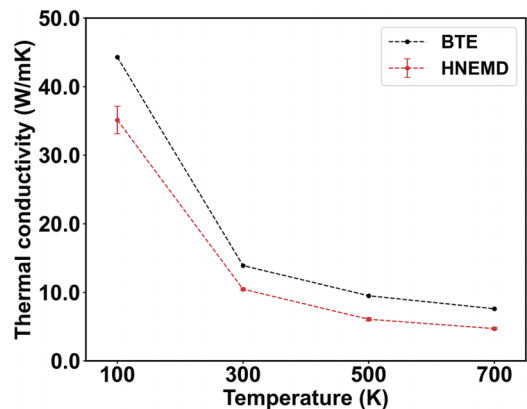

FIG. 3. In-plane thermal conductivity of monolayer $SrTiO_3$ from 100 to 700 K.
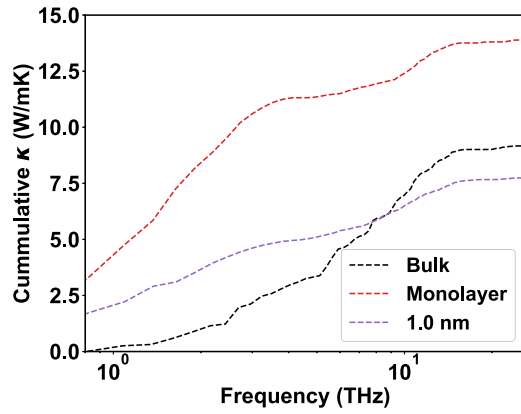
FIG. 4. In-plane cumulative thermal conductivity of the bulk, monolayer, and SrTiO$_3$ thin film with 1.0 nm thickness.

monolayer SrTiO$_3$, phonon modes below 1.8 THz contribute 50% to the thermal conductivity, while for bulk SrTiO$_3$, these phonon modes only contribute 15%, which implies the importance of low-frequency (long-wavelength) ZA phonon modes in the phonon transport of monolayer SrTiO$_3$. The transition of low-frequency acoustic phonon dispersion from bulk to monolayer SrTiO$_3$ alters both phonon properties and phonon scattering processes, leading to enhanced phonon conduction in monolayer SrTiO$_3$. Interestingly, the relation of thermal conductivity between bulk and monolayer SrTiO$_3$ resembles that between van der Waals materials and their 2D counterparts. For instance, the thermal conductivity of graphene is much higher than that of graphite [27,52].

IV. IN-PLANE PHONON TRANSPORT IN FREESTANDING STRONTIUM TITANATE THIN FILMS

For thicker films, the harmonic phonon dispersions show distinct imaginary frequency modes (see Fig. S3 [43]). In Fig. 5, using the TDEP method, we calculated the renormal-
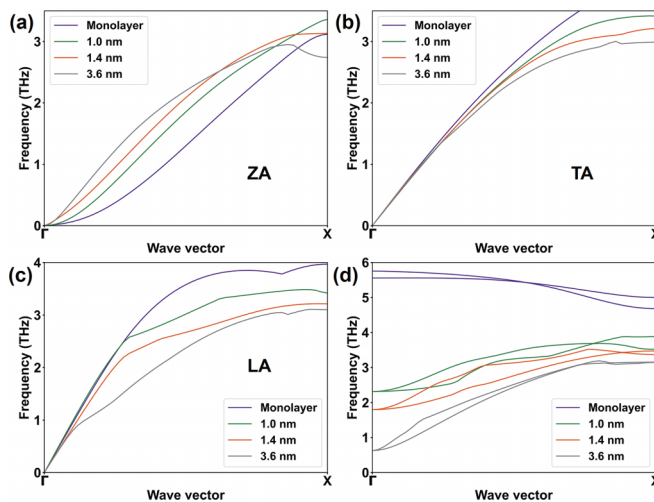

FIG. 5. Renormalized phonon dispersion relations of the (a) ZA, (b) TA, (c) longitudinal acoustic (LA), and (d) the lowest optical phonon branches along the Γ-X path of SrTiO$_3$ thin films with different thicknesses at 300 K.
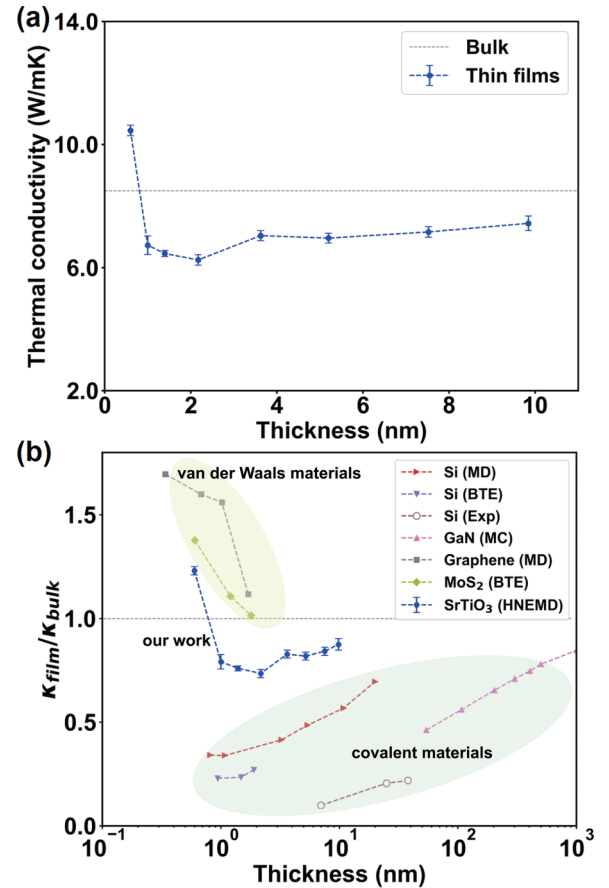

FIG. 6. (a) Thermal conductivity of SrTiO$_3$ thin films with different thicknesses at 300 K calculated from the HNEMD simulations. (b) Normalized thickness-dependent in-plane thermal conductivity ($\kappa_{film}/\kappa_{bulk}$) of different thin films including Si (MD [25], Exp [25], and BTE [22]), GaN [53], graphene [54], and MoS$_2$ [47]. Exp stands for experimental data, and MC represents Monte Carlo simulation.

ized phonon dispersions of monolayer SrTiO$_3$ and thin films with thicknesses of 1.0, 1.4, and 3.6 nm at 300 K (the acoustic and the lowest optical phonon branches along the Γ-X path are displayed; full range phonon dispersions are shown in Fig. S10 [43]). No imaginary frequency phonon modes are found, which demonstrates the lattice stability of SrTiO$_3$ thin films at 300 K. Moreover, the ZA phonon branches of SrTiO$_3$ thin films exhibit a clear thickness dependence, and along the Γ-X path, the ZA phonons largely harden as thickness increases. Such a hardening effect with thickness is also observed in Si thin films [22,25]. The phonon dispersion near the Γ point changes from a quadratic curve to one that includes a linear term. Therefore, the hardening effect can increase the phonon group velocity and influence the scattering processes of low-frequency acoustic phonons. In addition, the low-frequency optical phonon branches at the Γ point gradually approach zero frequency as thickness increases. With the NEP and HNEMD simulations, we calculated the in-plane thermal conductivities of SrTiO$_3$ thin films with thickness from the monolayer limit to 10 nm at 300 K, as plotted in Fig. 6(a) together with the bulk value calculated from the HNEMD simulations. In Fig. 6(b), we show the thickness-dependent normalized in-plane thermal conductivity of van der Waals

materials (graphene, MoS$_2$, and their multilayer counterparts) and covalent Si and GaN with smooth surfaces. The thermal conductivities of graphene and monolayer MoS$_2$ are much higher than their bulk values, and the in-plane thermal conductivity of van der Waals materials rapidly decreases towards their bulk values as thickness increases. For covalent solids such as Si and GaN, the in-plane thermal conductivities of thin films with smooth surfaces are all lower than their bulk values, and the in-plane thermal conductivity tends to increase and approach their bulk values as thickness increases. However, the thickness-dependent in-plane thermal conductivity of SrTiO$_3$ thin films is unique: The thermal conductivity of the monolayer is higher than that of bulk SrTiO$_3$, while other SrTiO$_3$ thin films have slightly lower thermal conductivities than the bulk value. As the thickness increases from the monolayer limit to 1.0 nm, the thermal conductivity abruptly decreases from 10.5 to 6.7 W/mK (in the BTE method, the calculated thermal conductivity is reduced from 13.9 to 7.7 W/mK). The minimal thermal conductivity is achieved at the thickness of 2.2 nm, and then the thermal conductivity slowly increases to the bulk value. With an increasing thickness of thin films, the hardening effect of the ZA phonon branch and the emergence of low-frequency optical phonon branches enlarge the possible phonon scattering channels, enhancing the phonon scattering strength of the dominant low-frequency phonons and lowering thermal conductivity. In Fig. 4, it is obvious that the contribution to the in-plane thermal conductivity is much reduced for the SrTiO$_3$ thin film with 1.0 nm thickness compared to the monolayer. As thickness keeps increasing, the low-frequency optical phonon branches at the Γ point have little room to decrease. The rise of phonon group velocity resulting from ZA phonon hardening becomes dominant, and thermal conductivity gradually approaches the bulk value. In Fig. S11(a) [43], we also plot the potential energy surfaces (PESs) with respect to the atomic displacements along the phonon eigenvector directions at 300 K corresponding to the lowest phonon modes at the M point for SrTiO$_3$ thin films with different thicknesses. For monolayer and 1.0-nm-thick SrTiO$_3$ thin film, the PESs are single well, while for thicker films, the PESs become double well. By examining the atomic

vibrational modes of different phonons at the M point, we find that the rotational vibration modes along the a (or b) axis of the [TiO$_6$] octahedra [see Fig. S11(b) [43]] appear when the thickness is larger than 1.0 nm, which is consistent with the variation of the PES from single well to double well. An analysis of the PES and atomic vibrational modes provides further insight into the highest thermal conductivity of monolayer SrTiO$_3$ among these thin films.

V. CONCLUSION

In summary, we have investigated the in-plane phonon transport in monolayer SrTiO$_3$ and ultrathin SrTiO$_3$ films with different thicknesses up to 10 nm by constructing an accurate machine-learning NEP. The renormalized phonon dispersion of monolayer SrTiO$_3$ is insensitive to temperature change, distinguished from its bulk counterpart. Using both the BTE method and HNEMD simulations, the thermal conductivity of monolayer SrTiO$_3$ is demonstrated to be higher than that of the bulk due to the changed ZA phonon branches and much-enhanced heat conduction of low-frequency phonon modes in monolayer SrTiO$_3$. The thickness-dependent in-plane thermal conductivity of SrTiO$_3$ thin films is also extracted from the HNEMD simulations. As the thickness increases from the monolayer limit to 10 nm, thermal conductivity first decreases abruptly and then increases slowly to approach the bulk value. The thickness-induced low-frequency ZA phonon branch hardening and optical phonon branch softening largely affect the acoustic phonon scattering channels and phonon group velocity, which account for the observed trend of thermal conductivity transitions. This work uncovers the transition of the thermal conductivity of SrTiO$_3$ thin films from the monolayer limit to 10 nm with first-principles accuracy and deepens the understanding of phonon transport in oxide perovskite thin films.

[1] Y.-Y. Sun, M. L. Agiorgousis, P. Zhang, and S. Zhang, Chalcogenide perovskites for photovoltaics, Nano Lett. **15**, 581 (2015).

[2] G. Grancini and M. K. Nazeeruddin, Dimensional tailoring of hybrid perovskites for photovoltaics, Nat. Rev. Mater. **4**, 4 (2019).

[3] H.-Y. Zhang, X.-J. Song, H. Cheng, Y.-L. Zeng, Y. Zhang, P.-F. Li, W.-Q. Liao, and R.-G. Xiong, A three-dimensional lead halide perovskite-related ferroelectric, J. Am. Chem. Soc. **142**, 4604 (2020).

[4] Y. Zhou, J. Wang, D. Luo, D. Hu, Y. Min, and Q. Xue, Recent progress of halide perovskites for thermoelectric application, Nano Energy **94**, 106949 (2022).

[5] Q. Wang, Z. Zeng, P. Zhao, C. Chen, N. Ouyang, J. Mao, and Y. Chen, B-site columnar-ordered halide double perovskites: Breaking octahedra motions induces strong lattice anharmonicity and thermal anisotropy, Chem. Mater. **35**, 1633 (2023).

[6] A. G. Ricciardulli, S. Yang, J. H. Smet, and M. Saliba, Emerging perovskite monolayers, Nat. Mater. **20**, 1325 (2021).

[7] S. G. Motti, T. Crothers, R. Yang, Y. Cao, R. Li, M. B. Johnston, J. Wang, and L. M. Herz, Heterogeneous photon recycling and charge diffusion enhance charge transport in quasi-2D lead-halide perovskite films, Nano Lett. **19**, 3953 (2019).

[8] F. Xia, H. Wang, D. Xiao, M. Dubey, and A. Ramasubramaniam, Two-dimensional material nanophotonics, Nat. Photonics **8**, 899 (2014).

[9] X. Qi, Y. Zhang, Q. Ou, S. T. Ha, C.-W. Qiu, H. Zhang, Y.-B. Cheng, Q. Xiong, and Q. Bao, Photonics and optoelectronics of 2D metal-halide perovskites, Small **14**, 1800682 (2018).

[10] J.-K. Huang, Y. Wan, J. Shi, J. Zhang, Z. Wang, W. Wang, N. Yang, Y. Liu, C.-H. Lin, X. Guan *et al.*, High-κ perovskite membranes as insulators for two-dimensional transistors, Nature (London) **605**, 262 (2022).

[11] D. Ji, S. Cai, T. R. Paudel, H. Sun, C. Zhang, L. Han, Y. Wei, Y. Zang, M. Gu, Y. Zhang *et al.*, Freestanding crystalline oxide perovskites down to the monolayer limit, Nature (London) **570**, 87 (2019).

[12] Z. Zhang and R. M. Wentzcovitch, *Ab initio* lattice thermal conductivity of MgSiO$_3$ across the perovskite-postperovskite phase transition, Phys. Rev. B **103**, 144103 (2021).

[13] Q. Wang, Z. Zeng, and Y. Chen, Revisiting phonon transport in perovskite SrTiO$_3$: Anharmonic phonon renormalization and four-phonon scattering, Phys. Rev. B **104**, 235205 (2021).

[14] L. Feng, T. Shiga, and J. Shiomi, Phonon transport in perovskite SrTiO$_3$ from first principles, Appl. Phys. Express **8**, 071501 (2015).

[15] Z. Zhang, K. Yuan, J. Zhu, X. Fan, J. Zhou, and D. Tang, Thermal conductivity of SrTiO$_3$ under high-pressure, Appl. Phys. Lett. **120**, 262201 (2022).

[16] O. Hellman, P. Steneteg, I. A. Abrikosov, and S. I. Simak, Temperature dependent effective potential method for accurate free energy calculations of solids, Phys. Rev. B **87**, 104111 (2013).

[17] O. Hellman, I. A. Abrikosov, and S. I. Simak, Lattice dynamics of anharmonic solids from first principles, Phys. Rev. B **84**, 180301(R) (2011).

[18] T. Tadano and S. Tsuneyuki, Self-consistent phonon calculations of lattice dynamical properties in cubic SrTiO$_3$ with first-principles anharmonic force constants, Phys. Rev. B **92**, 054301 (2015).

[19] X. Li, B. Fauqué, Z. Zhu, and K. Behnia, Phonon thermal Hall effect in strontium titanate, Phys. Rev. Lett. **124**, 105901 (2020).

[20] J.-J. Zhou, O. Hellman, and M. Bernardi, Electron-Phonon Scattering in the Presence of Soft Modes and Electron Mobility in SrTiO$_3$ Perovskite from first Principles, Phys. Rev. Lett. **121**, 226603 (2018).

[21] V. Martelli, J. L. Jiménez, M. Continentino, E. Baggio-Saitovitch, and K. Behnia, Thermal Transport and Phonon Hydrodynamics in Strontium Titanate, Phys. Rev. Lett. **120**, 125901 (2018).

[22] Q. Wang, R. Guo, C. Chi, K. Zhang, and B. Huang, Direct first-principle-based study of mode-wise in-plane phonon transport in ultrathin silicon films, Int. J. Heat Mass Transfer **143**, 118507 (2019).

[23] B. Fu, K. D. Parrish, H.-Y. Kim, G. Tang, and A. J. H. McGaughey, Phonon confinement and transport in ultrathin films, Phys. Rev. B **101**, 045417 (2020).

[24] M. Morita and T. Shiga, Surface phonons limit heat conduction in thin films, Phys. Rev. B **103**, 195418 (2021).

[25] S. Neogi, J. S. Reparaz, L. F. C. Pereira, B. Graczykowski, M. R. Wagner, M. Sledzinska, A. Shchepetov, M. Prunnila, J. Ahopelto, C. M. Sotomayor-Torres *et al.*, Tuning thermal transport in ultrathin silicon membranes by surface nanoscale engineering, ACS Nano **9**, 3820 (2015).

[26] E. Chávez-Ángel, J. S. Reparaz, J. Gomis-Bresco, M. R. Wagner, J. Cuffe, B. Graczykowski, A. Shchepetov, H. Jiang, M. Prunnila, J. Ahopelto *et al.*, Reduction of the thermal conductivity in free-standing silicon nano-membranes investigated by non-invasive Raman thermometry, APL Mater. **2**, 012113 (2014).

[27] Y. Kuang, L. Lindsay, and B. Huang, Unusual enhancement in intrinsic thermal conductivity of multilayer graphene by tensile strains, Nano Lett. **15**, 6121 (2015).

[28] X. Gu, Y. Wei, X. Yin, B. Li, and R. Yang, Colloquium: Phononic thermal properties of two-dimensional materials, Rev. Mod. Phys. **90**, 041002 (2018).

[29] P. Korotaev, I. Novoselov, A. Yanilkin, and A. Shapeev, Accessing thermal conductivity of complex compounds by machine learning interatomic potentials, Phys. Rev. B **100**, 144308 (2019).

[30] H. Dong, C. Cao, P. Ying, Z. Fan, P. Qian, and Y. Su, Anisotropic and high thermal conductivity in monolayer quasi-hexagonal fullerene: A comparative study against bulk phase fullerene, Int. J. Heat Mass Transfer **206**, 123943 (2023).

[31] J. Tang, G. Li, Q. Wang, J. Zheng, L. Cheng, and R. Guo, Competition between phonon-vacancy and four-phonon scattering in cubic boron arsenide by machine learning interatomic potential, Phys. Rev. Mater. **7**, 044601 (2023).

[32] C. Mangold, S. Chen, G. Barbalinardo, J. Behler, P. Pochet, K. Termentzidis, Y. Han, L. Chaput, D. Lacroix, and D. Donadio, Transferability of neural network potentials for varying stoichiometry: Phonons and thermal conductivity of Mn$_x$Ge$_y$ compounds, J. Appl. Phys. **127**, 244901 (2020).

[33] X. Qian and R. Yang, Machine learning for predicting thermal transport properties of solids, Mater. Sci. Eng, R **146**, 100642 (2021).

[34] Y. Luo, M. Li, H. Yuan, H. Liu, and Y. Fang, Predicting lattice thermal conductivity via machine learning: a mini review, npj Comput. Mater. **9**, 4 (2023).

[35] Z. Fan, Z. Zeng, C. Zhang, Y. Wang, K. Song, H. Dong, Y. Chen, and T. Ala-Nissila, Neuroevolution machine learning potentials: Combining high accuracy and low cost in atomistic simulations and application to heat transport, Phys. Rev. B **104**, 104309 (2021).

[36] Z. Fan, Y. Wang, P. Ying, K. Song, J. Wang, Y. Wang, Z. Zeng, K. Xu, E. Lindgren, J. M. Rahm *et al.*, GPUMD: A package for constructing accurate machine-learned potentials and performing highly efficient atomistic simulations, J. Chem. Phys. **157**, 114801 (2022).

[37] D. J. Evans, Homogeneous NEMD algorithm for thermal conductivity–Application of non-canonical linear response theory, Phys. Lett. A **91**, 457 (1982).

[38] P. E. Blöchl, Projector augmented-wave method, Phys. Rev. B **50**, 17953 (1994).

[39] J. P. Perdew, A. Ruzsinszky, G. I. Csonka, O. A. Vydrov, G. E. Scuseria, L. A. Constantin, X. Zhou, and K. Burke, Restoring the Density-Gradient Expansion for Exchange in Solids and Surfaces, Phys. Rev. Lett. **100**, 136406 (2008).

[40] K. Gubaev, E. V. Podryabinkin, G. L. Hart, and A. V. Shapeev, Accelerating high-throughput searches for new alloys with active learning of interatomic potentials, Comput. Mater. Sci. **156**, 148 (2019).

[41] G. Kresse and J. Furthmüller, Efficient iterative schemes for *ab initio* total-energy calculations using a plane-wave basis set, Phys. Rev. B **54**, 11169 (1996).

[42] S. Plimpton, Fast parallel algorithms for short-range molecular dynamics, J. Comput. Phys. **117**, 1 (1995).

[43] See Supplemental Material at http://link.aps.org/supplemental/10.1103/PhysRevB.108.115435 for the validation of the NEP, details of the BTE calculations, details of the HNEMD simulations, and potential energy surface, which includes Refs. [37,55,56].

[44] A. Togo and I. Tanaka, First principles phonon calculations in materials science, Scr. Mater. **108**, 1 (2015).

[45] W. Li, J. Carrete, N. A. Katcho, and N. Mingo, ShengBTE: A solver of the Boltzmann transport equation for phonons, Comput. Phys. Commun. **185**, 1747 (2014).

[46] Z. Han, X. Yang, W. Li, T. Feng, and X. Ruan, Four-Phonon: An extension module to ShengBTE for computing four-phonon scattering rates and thermal conductivity, Comput. Phys. Commun. **270**, 108179 (2022).

[47] X. Gu, B. Li, and R. Yang, Layer thickness-dependent phonon properties and thermal conductivity of MoS₂, J. Appl. Phys. **119**, 085106 (2016).

[48] N. Bonini, J. Garg, and N. Marzari, Acoustic phonon lifetimes and thermal transport in free-standing and strained graphene, Nano Lett. **12**, 2673 (2012).

[49] J. Carrete, W. Li, L. Lindsay, D. A. Broido, L. J. Gallego, and N. Mingo, Physically founded phonon dispersions of few-layer materials and the case of borophene, Mater. Res. Lett. **4**, 204 (2016).

[50] S. R. Popuri, A. Scott, R. Downie, M. Hall, E. Suard, R. Decourt, M. Pollet, and J.-W. Bos, Glass-like thermal conductivity in SrTiO₃ thermoelectrics induced by A-site vacancies, RSC Adv. **4**, 33720 (2014).

[51] Q. Wang, R. Guo, B. Huang, and Y. Chen, Unusual width dependence of lattice thermal conductivity in ultranarrow armchair graphene nanoribbons with unpassivated edges, J. Phys. Chem. C **125**, 6034 (2021).

[52] G. Fugallo, A. Cepellotti, L. Paulatto, M. Lazzeri, N. Marzari, and F. Mauri, Thermal conductivity of graphene and graphite: collective excitations and mean free paths, Nano Lett. **14**, 6109 (2014).

[53] R. Wu, R. Hu, and X. Luo, First-principle-based full-dispersion Monte Carlo simulation of the anisotropic phonon transport in the wurtzite GaN thin film, J. Appl. Phys. **119**, 145706 (2016).

[54] Z. Wei, Z. Ni, K. Bi, M. Chen, and Y. Chen, In-plane lattice thermal conductivities of multilayer graphene films, Carbon **49**, 2653 (2011).

[55] G. Bussi and M. Parrinello, Accurate sampling using Langevin dynamics, Phys. Rev. E **75**, 056707 (2007).

[56] F. Eriksson, E. Fransson, and P. Erhart, The Hiphive package for the extraction of high-order force constants by machine learning, Adv. Theory Simul. **2**, 1800184 (2019).